Dynamic Modeling Methodologies for Inductive Power Transfer Systems: A Comparative Review

Sangmin Lee, *Member, IEEE*, Lars Cronje Bjorndal, *Student Member, IEEE*, Naser Vosoughi Kurdkandi, *Member, IEEE*, Ching-Ming Lai, *Senior Member, IEEE*, and Chunting Chris Mi, *Fellow, IEEE*

***Abstract*—Inductive power transfer (IPT) systems feature dynamic behaviors due to high-quality-factor resonant tanks, nonlinear rectifier behavior, and both fast switching and slow envelope dynamics, making accurate dynamic modeling challenging. Although numerous modeling techniques have been proposed, their dynamic characteristics, applicability, and limitations have not been systematically compared. To bridge this gap, this paper presents a unified benchmark comparison of three representative dynamic modeling approaches for series–series compensated IPT systems: the Extended Describing Function (EDF), Generalized State-Space Averaging (GSSA), and Rotating Reference Frame (RRF) models. Moving beyond a conventional narrative review, this study establishes clear evaluation metrics—including transient response accuracy, settling-time prediction, stability margins, and structural complexity—to deliver a definitive model-selection guidance for control-oriented IPT analysis. The detailed quantitative evaluation is confined to the SS-IPT topology, which serves as a representative resonant structure for fundamental-frequency modeling. Within this framework, the models are compared in terms of transient response accuracy, settling-time prediction, structural complexity, and cross-coupling behavior, with particular emphasis on their applicability under load, frequency, and coupling variations. Furthermore, simulation-based comparisons are performed to assess their dynamic fidelity, including the critical effects of rectifier-capacitor dynamics on envelope tracking. The results highlight the mathematical and computational trade-offs among the three modeling techniques, establishing a unified benchmarking framework that provides systematic guidance for selecting an appropriate model according to the required level of fidelity and application needs.**

***Index Terms*—Inductive power transfer system, dynamic modeling, extended describing function, generalized state-space averaging, rotating reference frame.**

Received 17 December 2025; revised 23 February 2026; 6 April 2026 and 19 May 2026; accepted 18 June 2026. The associate editor coordinating the review of this article and approving it for publication was Dr. Alireza Safaee. *(Corresponding author: Chunting Chris Mi.)*

Sangmin Lee, Lars Cronje Bjorndal, Naser Vosoughi Kurdkandi, and Chunting Chris Mi are with the Department of Electrical and Computer Engineering, San Diego State University, San Diego, CA 92182 USA.

Ching-Ming Lai is with the Department of Electrical Engineering, National Chung Hsing University, Taichung City 402, Taiwan (e-mail: mi@ieee.org).

Digital Object Identifier 10.1109/JWPT.2026.3708071

I. Introduction

INDUCTIVE power transfer (IPT) systems have gained increasing prominence in applications such as consumer electronics, industrial and electric transportation systems due to their electrical isolation, mechanical robustness, and convenience [1], [2], [3], [4], [5], [6], [7]. Unlike wired converters, IPT systems rely on magnetically coupled resonant tanks whose characteristics are strongly influenced by mutual inductance, coil alignment, load conditions, and operating frequency. Such dependencies introduce dynamic behaviors that cannot be captured by steady-state analysis alone. As a result, transient responses become especially important as IPT systems advance toward high-power and safety-critical domains, where undesirable dynamic excursions may cause voltage overshoot, current stress, or loss of soft switching [8], [9], [10]. Consequently, dynamic-domain modeling has become an essential tool for ensuring stable and predictable operation under practical operating conditions.

Historically, research on IPT systems has primarily focused on hardware-level enhancements—such as compensation-network topologies, magnetic-coupling improvement, and coil design optimization—to increase efficiency and widen the operating range [2], [11], [12], [13], [14]. Although these developments have significantly advanced performance under steady-state conditions, they provide limited insight into the transient phenomena that arise during rapid variations in coupling, load, or excitation.

Correspondingly, the modeling of IPT systems has evolved from steady-state phasor-domain representations to increasingly dynamic and control-oriented frameworks. Early phasor-based models facilitated efficient evaluation of power-transfer characteristics and compensation behavior but were unable to describe large-signal or switching-induced transients [15], [16], [17], [18]. To improve fidelity beyond steady-state representations, time-domain differential-equation models were introduced to capture the full dynamics of the coupled resonant tanks [19], [20], [21]. However, directly simulating these switching-waveform–based models incurs substantial computational burden, limiting their practicality for analysis and control design.

To mitigate this challenge, the Extended Describing Function (EDF) method was later employed to approximate the nonlinear inverter switching action in the harmonic domain, thereby retaining essential switching effects while yielding a more tractable dynamic model for resonant systems [22], [23], [24], [25], [26], [27]. However, EDF models retain substantial structural complexity, which makes analytical manipulation and control-oriented simplification challenging. This motivated the development of reduced-order techniques such as generalized state-space averaging (GSSA), which incorporate switching effects through harmonic balancing and averaging to produce a simpler representation of the resonant dynamics [28], [29], [30], [31], [32], [33], [34]. Nevertheless, GSSA remains in the stationary reference frame, so the carrier-frequency–induced cross-coupling inherent to sinusoidal basis functions persists. To address this limitation, rotating-reference-frame (RRF) models were introduced to eliminate these frequency-dependent coupling terms and yield low-frequency equivalents more suitable for control-oriented analysis [35], [36], [37], [38], [39], [40]. Collectively, these developments reflect the field's transition from steady-state, circuit-centric approaches toward dynamic, frequency-aware modeling techniques capable of describing the increasingly demanding transient behavior of modern IPT systems.

Beyond these physics-based modeling approaches, recent work has explored artificial intelligence and neural-network–based system identification for IPT systems, wherein nonlinear dynamics are learned directly from data rather than derived from analytical circuit formulations [41], [42], [43], [44]. Such data-driven models—including feedforward architectures and recurrent networks—have demonstrated potential in capturing switching nonlinearities, frequency-dependent coupling effects, and misalignment-induced parameter variations. More recently, hybrid and physics-informed learning frameworks have been proposed to incorporate physical constraints into data-driven architectures, suggesting promising directions for integrating analytical structure with learning-based methods. However, because these approaches rely on algorithmic training rather than first-principles derivation and remain at a relatively early stage with limited analytical interpretability, they fall outside the scope of this review, which focuses instead on established analytical modeling approaches that explicitly describe resonant dynamics through circuit-derived formulations.

Despite significant analytical developments, the dynamic behavior of IPT systems—and the modeling frameworks used to analyze them—has not been comprehensively compared in existing review papers [45], [46], [47], [48], [49]. To address these limitations, this paper presents a unified benchmark study of the EDF, GSSA, and RRF methodologies for SS-IPT systems, tracing their evolutionary trajectory from steady-state approximations to full dynamic models. Each approach is rigorously evaluated based on transient accuracy, settling-time prediction, structural complexity, and cross-coupling behavior, providing systematic, control-oriented model-selection guidance.

The remainder of this paper is organized as follows. Section II presents unified derivations and formulation principles for the EDF, GSSA, and RRF dynamic models. Section III presents a comprehensive comparison of the three models, including their transient and steady-state accuracy, dynamic fidelity, structural complexity, generality under varying operating conditions, and applicability for control-oriented analysis. Section IV summarizes the key insights and outlines potential directions for future research.

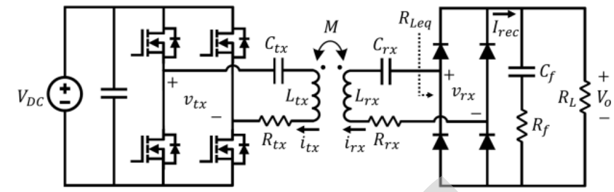

Fig. 1. An equivalent circuit of series-series tuned IPT system.

II. Unified Dynamic Modeling of SS-IPT Systems

This section introduces the EDF, GSSA, and RRF models of the SS-IPT system. Fig. 1 illustrates the equivalent circuit of the SS-IPT system. The full-bridge inverter converts the DC voltage into a high-frequency AC voltage, driving a high-frequency current through the transmitter coil. This induces a voltage in the magnetically coupled receiver coil, which generates a high-frequency AC current according to the load, and the rectifier converts it into a DC output supplied to the load. Although the inverter output voltage is a square waveform, all three models assume high-quality-factor resonant tanks, allowing the application of the fundamental harmonic approximation (FHA). Under this assumption, only the first harmonic component of the inverter output voltage is considered, while all higher-order harmonics are neglected. The inverter is assumed to operate as a full-bridge converter under duty-ratio modulation, generating a three-level square-wave voltage $v_{tx}(t)$ as shown in Fig. 3. The duty ratio D determines the effective pulse width within each switching period. Under the FHA, only the first harmonic component of this square waveform is retained, whose amplitude is given by $4V_{DC}\sin(\pi D)/\pi$ as expressed in (1).

$$v_{tx,1}(t) = \frac{4V_{DC}}{\pi}\sin(\pi D)\,sin(\omega_0 t) \tag{1}$$

where V_{DC} denotes the DC-link voltage of the inverter and ω_0 represents the operating frequency.

To clarify the mathematical notations used in the subsequent sections, the subscripts for the state variables in each dynamic model are defined based on their respective orthogonal components. Specifically, subscripts 's' and 'c' denote the sine and cosine components in the EDF model, 'r' and 'i' represent the real and imaginary parts in the GSSA model, and 'd' and 'q' correspond to the d- and q-axis variables in the RRF model.

A. Extended Describing Function (EDF)

EDF modeling uses harmonic-balance–based fundamental approximation to replace the nonlinear switching behavior with an equivalent fundamental-frequency representation, enabling large-signal and small-signal dynamic modeling with high fidelity. Z. U. Zahid presented the modeling procedure for the EDF model of the SS-IPT system [22]. However, the referenced

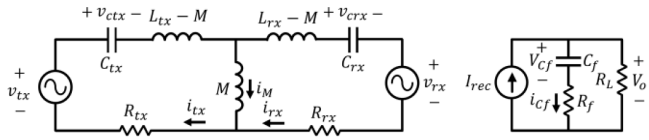

Fig. 2. T-equivalent model of the series-series tuned IPT system.

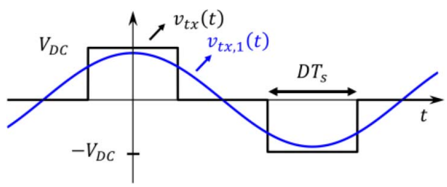

Fig. 3. Inverter output voltage and fundamental waveform.

work does not incorporate the transmitter and receiver winding resistances R_{tx} and R_{rx}. In this study, these winding resistances are explicitly included not only to improve the model accuracy but also to ensure a consistent basis for comparison with the other dynamic modeling approaches. Fig. 2 shows the T-equivalent model; the transformer turns ratio is 1:1. v_{rx} denotes the fundamental component of the receiver coil voltage obtained by applying the FHA, and i_{rec} represents the rectified current after the full-wave rectifier. By applying Kirchhoff's voltage law (KVL) to the transmitter and receiver coils in the circuit of Fig. 2, the following equations can be derived.

$$v_{tx} = v_{ctx} + L_{tx}\frac{di_{tx}}{dt} + R_{tx}i_{tx} - M\frac{di_{rx}}{dt} \tag{2}$$

$$v_{rx} = v_{crx} + L_{rx}\frac{di_{rx}}{dt} + R_{rx}i_{rx} - M\frac{di_{tx}}{dt} \tag{3}$$

The differential equations for i_{tx} and i_{rx} can be derived using (2)–(3) and are expressed as follows.

$$\begin{aligned}\frac{di_{tx}}{dt} &= \frac{L_{rx}}{\Delta}[v_{tx} - v_{ctx}] + \frac{M}{\Delta}[v_{rx} - v_{crx}]\\ &\quad - \frac{L_{rx}}{\Delta}R_{tx}i_{tx} - \frac{M}{\Delta}R_{rx}i_{rx}\end{aligned} \tag{4}$$

$$\begin{aligned}\frac{di_{rx}}{dt} &= \frac{L_{tx}}{\Delta}[v_{rx} - v_{crx}] + \frac{M}{\Delta}[v_{tx} - v_{ctx}]\\ &\quad - \frac{L_{tx}}{\Delta}R_{rx}i_{rx} - \frac{M}{\Delta}R_{tx}i_{tx}\end{aligned} \tag{5}$$

where Δ represents the coupling condition; ($\Delta > 0$) ensures the magnetic energy of the system remains positive. Δ is defined as $L_{tx}L_{rx} - M^2$. In these equations, the first and second terms represent the voltages across the coils and tuning capacitors, while the third and fourth terms correspond to the voltage drops caused by the coil winding resistances. By applying Kirchhoff's current law (KCL) to the rectifier equivalent circuit in Fig. 2, the expressions for the rectifier capacitor voltage and the output voltage can be derived as follows.

$$I_{rec} = C_f\left(1 + \frac{R_f}{R_L}\right)\frac{dV_{cf}}{dt} + \frac{V_{cf}}{R_L} \tag{6}$$

$$V_o = \frac{R_f R_L}{R_f + R_L}I_{rec} + \frac{R_L}{R_L + R_f}V_{cf} \tag{7}$$

where V_{cf} denotes the voltage across the rectifier capacitor. R_f denotes the equivalent series resistance (ESR) of the rectifier output capacitor C_f. It is introduced to provide a more refined representation of the capacitor dynamics; however, it is not essential to the fundamental modeling framework and may be neglected without affecting the core formulation. R_L represents the equivalent load resistance. I_{rec} denotes the rectifier output current, and V_o represents the output voltage. Since all AC voltages and currents in the SS-IPT system are assumed to contain only the fundamental components, they can be generally expressed as the sum of sine and cosine terms through Fourier series expansion. However, by assuming the input voltage $v_{tx,1}$ as the reference for all voltage and current components, it can be represented as having only a sine component, as expressed in (1). Due to the rectifier operation, the receiver coil voltage becomes $+V_o$ when i_{rx} is positive and $-V_o$ when i_{rx} is negative. Assuming $R_c \ll R_L$, such that the voltage drop caused by the rectifier capacitor ESR is negligible, v_{rx} can be expressed through Fourier expansion as given in (8). Since the v_{rx} has a phase difference with the input voltage v_{tx}, it contains both sine and cosine terms.

$$v_{rx} = \frac{4}{\pi}\frac{V_{Cf}}{\sqrt{i_{rx,s}^2 + i_{rx,c}^2}}[i_{rx,s}\sin(\omega_0 t) + i_{rx,c}\cos(\omega_0 t)] \tag{8}$$

It should be noted that the subscripts 's' and 'c' denote the sine and cosine terms of the time-varying envelope, respectively. These variables characterize the dynamic response of the current by capturing the slow modulation of its amplitude and phase. The expression written as the sum of sine and cosine terms constitutes the standard state equation of the EDF model. Similarly, by decomposing the voltages and currents of the SS-IPT system into their fundamental sine and cosine components based on (1)–(8), the following dynamic equations can be derived.

$$\begin{aligned}\frac{di_{tx,s}}{dt} &= \frac{L_{rx}}{\Delta}(V_e - v_{ctx,s}) - \frac{M}{\Delta}(v_{rx,s} + v_{crx,s})\\ &\quad - \frac{L_{rx}}{\Delta}R_{tx}i_{tx,s} - \frac{M}{\Delta}R_{rx}i_{rx,s} + \omega_0 i_{tx,c}\end{aligned} \tag{9}$$

$$\begin{aligned}\frac{di_{rx,s}}{dt} &= \frac{M}{\Delta}(V_e - v_{ctx,s}) - \frac{L_{tx}}{\Delta}(v_{rx,s} + v_{crx,s})\\ &\quad - \frac{M}{\Delta}R_{tx}i_{tx,s} - \frac{L_{tx}}{\Delta}R_{rx}i_{rx,s} + \omega_0 i_{rx,c}\end{aligned} \tag{10}$$

$$\frac{dv_{ctx,s}}{dt} = \frac{i_{tx,s}}{C_{tx}} + \omega_0 v_{ctx,c} \tag{11}$$

$$\frac{dv_{crx,s}}{dt} = \frac{i_{rx,s}}{C_{rx}} + \omega_0 v_{crx,c} \tag{12}$$

$$v_{rx,s} = \frac{4}{\pi}\frac{i_{rx,s}}{\sqrt{i_{rx,s}^2 + i_{rx,c}^2}}V_{Cf} \tag{13}$$

$$\frac{di_{tx,c}}{dt} = -\frac{L_{rx}}{\Delta}v_{ctx,c} - \frac{M}{\Delta}(v_{rx,c} + v_{crx,c}) - \frac{L_{rx}}{\Delta}R_{tx}i_{tx,c} - \frac{M}{\Delta}R_{rx}i_{rx,c} - \omega_0 i_{tx,s} \quad (14)$$

$$\frac{di_{rx,c}}{dt} = -\frac{M}{\Delta}v_{ctx,c} - \frac{L_{tx}}{\Delta}(v_{rx,c} + v_{crx,c}) - \frac{M}{\Delta}R_{tx}i_{tx,c} - \frac{L_{tx}}{\Delta}R_{rx}i_{rx,c} - \omega_0 i_{rx,s} \quad (15)$$

$$\frac{dv_{ctx,c}}{dt} = \frac{i_{tx,c}}{C_{tx}} - \omega_0 v_{ctx,s} \quad (16)$$

$$\frac{dv_{crx,c}}{dt} = \frac{i_{rx,c}}{C_{rx}} - \omega_0 v_{crx,s} \quad (17)$$

$$v_{rx,c} = \frac{4}{\pi}\frac{i_{rx,c}}{\sqrt{i_{rx,s}^2 + i_{rx,c}^2}}V_{Cf} \quad (18)$$

where V_e is defined as $4V_{DC} \cdot \sin(\pi D)/\pi$. Using $I_{rec} \approx 2/\pi \cdot \sqrt{i_{rx,s}^2 + i_{rx,c}^2}$, the rectifier capacitor voltage V_{cf} and the output voltage V_o can be expressed as follows:

$$\frac{dV_{Cf}}{dt} = \frac{1}{C_f}\left[\frac{2}{\pi}\frac{R_L}{R_f + R_L}\sqrt{i_{rx,s}^2 + i_{rx,c}^2} - \frac{1}{R_f + R_L}V_{Cf}\right] \quad (19)$$

$$V_o = \frac{2}{\pi}\frac{R_f R_L}{R_f + R_L}\sqrt{i_{rx,s}^2 + i_{rx,c}^2} + \frac{R_L}{R_f + R_L}V_{Cf} \quad (20)$$

Equations (9)–(20) represent a dynamic model that accurately tracks the voltage and current envelopes of the SS-IPT system, enabling precise characterization of both transient and steady-state response.

If the nonlinear terms are to be eliminated and the modeling simplified, the full-wave rectifier as seen from the receiver coil can be represented by an equivalent resistance. The load resistance R_L in Fig. 1 and the equivalent resistance of the rectifier as seen from the receiver coil can be expressed as (21).

$$R_{Leq} = \frac{8}{\pi^2}R_L \quad (21)$$

With this assumption, the equivalent circuit of the SS-IPT system can be expressed as shown in Fig. 4 [50]. In this case, the expressions in (9), (10), (14), and (15) are modified as follows.

$$\frac{di_{tx,s}}{dt} = \frac{L_{rx}}{\Delta}(V_e - v_{ctx,s}) - \frac{M}{\Delta}v_{crx,s} - \frac{L_{rx}}{\Delta}R_{tx}i_{tx,s} - \frac{M}{\Delta}(R_{rx} + R_{Leq})i_{rx,s} + \omega_0 i_{tx,c} \quad (22)$$

$$\frac{di_{rx,s}}{dt} = \frac{M}{\Delta}(V_e - v_{ctx,s}) - \frac{L_{tx}}{\Delta}v_{crx,s} - \frac{M}{\Delta}R_{tx}i_{tx,s} - \frac{L_{tx}}{\Delta}(R_{rx} + R_{Leq})i_{rx,s} + \omega_0 i_{rx,c} \quad (23)$$

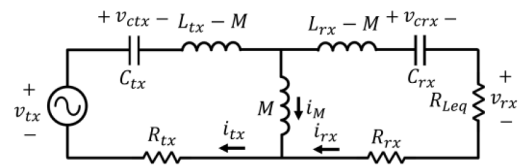

Fig. 4. T-equivalent model of the series-series tuned IPT system using the rectifier equivalent circuit.

$$\frac{di_{tx,c}}{dt} = -\frac{L_{rx}}{\Delta}v_{ctx,c} - \frac{M}{\Delta}v_{crx,c} - \frac{L_{rx}}{\Delta}R_{tx}i_{tx,c} - \frac{M}{\Delta}(R_{rx} + R_{Leq})i_{rx,c} - \omega_0 i_{tx,s} \quad (24)$$

$$\frac{di_{rx,c}}{dt} = -\frac{M}{\Delta}v_{ctx,c} - \frac{L_{tx}}{\Delta}v_{crx,c} - \frac{M}{\Delta}R_{tx}i_{tx,c} - \frac{L_{tx}}{\Delta}(R_{rx} + R_{Leq})i_{rx,c} - \omega_0 i_{rx,s} \quad (25)$$

Assuming an ideal full-wave rectifier and a sufficiently large rectifier capacitor, the output voltage V_o can be expressed as (26).

$$V_o = \frac{\pi}{4}R_{Leq}\sqrt{i_{rx,s}^2 + i_{rx,c}^2} \quad (26)$$

Therefore, the model can be simplified to an 8th-order system, which is one order lower than the model that includes the rectifier dynamics. The EDF formulation is well suited for resonant WPT systems, where power transfer is predominantly governed by the fundamental harmonic due to the high-quality-factor of the resonant tanks. Because higher-order harmonics are significantly attenuated by the resonant network, retaining only the dominant harmonic components enables EDF to accurately capture the essential energy-transfer dynamics.

B. Generalized State-Space Averaging (GSSA)

The key concept of the GSSA modeling technique is based on the assumption that voltage and current variations within a switching period are negligible, enabling model simplification through period averaging. Specifically, the GSSA method decomposes the voltages and currents of the SS-IPT system into their fundamental and harmonic components, averages out all higher-order harmonics except the fundamental, and thereby derives a slow-time-scale state-space model. The main difference between the EDF and GSSA methods is that the EDF models the system's fundamental-frequency dynamics using harmonic envelopes, whereas the GSSA represents the averaged behavior over a switching period under the assumption of a high switching frequency. By averaging out the harmonic components, a slow dynamic state-space model is obtained in which high-frequency terms are eliminated, thereby achieving an effect equivalent to that of applying the FHA, similar to the EDF method.

The full-wave rectifier, as seen from the receiver coil, is represented by an equivalent resistance as shown in Fig. 4. All voltages and currents in the SS-IPT system can be expressed in the form of a Fourier series as follows.

$$x(t) = \sum_{n=-\infty}^{\infty} X_n(t)e^{jn\omega_0 t} \tag{27}$$

where $x(t)$ represents the actual state variable in the time domain, and the index n indicates the harmonic order. $X_n(t)$ denotes the complex coefficient of the n-th Fourier series term obtained by expanding $x(t)$ in the frequency domain, corresponding to the envelope of the state variable. By differentiating (27), the expression in (28) can be obtained, which represents the form of the differential equation.

$$\frac{dx}{dt} = \sum_{n=-\infty}^{\infty} \left(\frac{dX_n}{dt} + jn\omega_0 X_n\right)e^{jn\omega_0 t} \tag{28}$$

Building on this representation, the GSSA framework proceeds by extracting the slowly varying envelopes $X_n(t)$ through a projection of (28) onto the corresponding harmonic subspaces. This projection is performed using the generalized averaging operator shown in (29).

$$\langle x(t)\rangle_k = \frac{1}{T_0}\int_0^{T_0} x(t)e^{-jk\omega_0 t}dt \tag{29}$$

This operator isolates the k-th harmonic component by exploiting the orthogonality of the exponential basis functions over one switching period. Applying this operator to (28) filters out all but the k-th harmonic term, yielding the standard GSSA state equation in (30).

$$\left\langle \frac{dx}{dt}\right\rangle_k = \frac{dX_k}{dt} + jk\omega_0 X_k \tag{30}$$

It should be noted that $X_0(t)$ and $X_1(t)$ represent the DC component and the complex amplitude of the fundamental component, respectively, while higher-order harmonics are neglected due to their minimal contribution to the low-frequency dynamics. Therefore, the complex coefficients of the fundamental components of the currents and voltages in Fig. 4 can be defined as follows.

$$I_{tx} = i_{tx,r} + ji_{tx,i} \tag{31}$$

$$I_{rx} = i_{rx,r} + ji_{rx,i} \tag{32}$$

$$V_{ctx} = v_{ctx,r} + jv_{ctx,i} \tag{33}$$

$$V_{crx} = v_{crx,r} + jv_{crx,i} \tag{34}$$

I_{tx} and I_{rx} denote the fundamental complex coefficients of the transmitter and receiver coil currents, respectively. V_{ctx} and V_{crx} represent the fundamental complex coefficients of the tuning capacitor voltages in the transmitter and receiver coils, respectively. The subscript 'r' and 'i' denote the real and imaginary coefficient of the time-varying envelope, respectively. By applying KVL to the equivalent circuit in Fig. 4 and separating the real and imaginary parts using (31)–(34), the GSSA model of the SS-IPT system can be obtained as follows.

$$\frac{di_{tx,r}}{dt} = -\frac{1}{L_{tx}}\left[R_{tx}i_{tx,r} + v_{ctx,r} + \omega_0 M i_{rx,i}\right] + \omega_0 i_{tx,i} \tag{35}$$

$$\frac{di_{tx,i}}{dt} = -\frac{1}{L_{tx}}\left[\frac{V_e}{2} + R_{tx}i_{tx,i} + v_{ctx,i} - \omega_0 M i_{rx,r}\right] - \omega_0 i_{tx,r} \tag{36}$$

$$\frac{dv_{ctx,r}}{dt} = \frac{1}{C_{tx}}i_{tx,r} + \omega_0 v_{ctx,i} \tag{37}$$

$$\frac{dv_{ctx,i}}{dt} = \frac{1}{C_{tx}}i_{tx,i} - \omega_0 v_{ctx,r} \tag{38}$$

$$\frac{dv_{crx,r}}{dt} = \frac{1}{C_{rx}}i_{rx,r} + \omega_0 v_{crx,i} \tag{39}$$

$$\frac{dv_{crx,i}}{dt} = \frac{1}{C_{rx}}i_{rx,i} - \omega_0 v_{crx,r} \tag{40}$$

$$\frac{di_{rx,r}}{dt} = -\frac{1}{L_{rx}}\left[\omega_0 M i_{tx,i} + v_{crx,r} + (R_{rx} + R_{Leq})i_{rx,r}\right] + \omega_0 i_{rx,i} \tag{41}$$

$$\frac{di_{rx,i}}{dt} = \frac{1}{L_{rx}}\left[\omega_0 M i_{tx,r} - v_{crx,i} - (R_{rx} + R_{Leq})i_{rx,i}\right] - \omega_0 i_{rx,r} \tag{42}$$

In the GSSA model, each state variable corresponds to a dynamic phasor rather than an instantaneous waveform. Therefore, to obtain the continuous-time envelope representing the peak value of the fundamental component, the following reconstruction equation is used.

$$x_{k,peak} = 2|X_k| = 2\sqrt{x_{k,r}^2 + x_{k,i}^2} \tag{43}$$

C. Rotational Reference Frame (RRF)

The dq RRF modeling approach represents IPT systems in a synchronous RRF aligned with the fundamental excitation. By transforming the time-domain voltages and currents into orthogonal d- and q-axis components, the RRF model converts sinusoidal state variables into slowly varying or nearly DC state waveforms. Unlike GSSA approaches, the RRF model does not rely on averaging-based simplifications. Instead, it preserves the original system dynamics and represents them in an RRF, yielding a full-order model that captures the mutual and cross-coupled interactions of the resonant tanks without modifying the underlying differential equations.

S. Lee detailed the design procedure of the RRF model for the SS-IPT system [35]. The dq transformation of a three-phase system into the RRF is performed by first converting the three-phase state variables into two-phase signals in a stationary reference frame (SRF) with a 90° phase difference using the Clarke transformation and then applying the Park transformation to obtain the RRF signals. However, because the IPT system in Fig. 1 is a single-phase system, the dq transformation used in three-phase systems cannot be directly applied. To achieve this, virtual signals with a 90° phase shift relative to the actual waveforms are artificially generated, producing an effect equivalent to the Clarke transformation in a three-phase system. This process yields a two-phase representation of the SS-IPT system in the SRF. By removing the time-varying rotational component, all voltages and currents of the SS-IPT system can be represented in the RRF.

The voltages and currents in Fig. 4 can be expressed as (44)–(46). These are the actual voltages and currents applied to the circuit, and they are defined as the d-axis components.

$$v^s_{tx,d} = V_e \cos(\omega_0 t) \tag{44}$$

$$i^s_{tx,d} = I_{tx} \cos(\omega_0 t - \phi_{tx}) \tag{45}$$

$$i^s_{rx,d} = I_{rx} \cos(\omega_0 t - \phi_{rx}) \tag{46}$$

The subscript 'd' and 'q' represent the d- and q-axis components of the state variables. The superscript 's' indicates that the variable is expressed in the SRF. The virtual voltage and current signals with a 90° phase shift can be expressed as follows, and these are defined as the q-axis components.

$$v^s_{tx,q} = V_e \sin(\omega_0 t) \tag{47}$$

$$i^s_{tx,q} = I_{tx} \sin(\omega_0 t - \phi_{tx}) \tag{48}$$

$$i^s_{rx,q} = I_{rx} \sin(\omega_0 t - \phi_{rx}) \tag{49}$$

By multiplying (48)–(51) by the unit imaginary number j and applying Euler's formula together with (52), the voltage equations of the SS-IPT system in the SRF can be expressed as (50) and (51). The superscript 'e' indicates that the variable is expressed in the RRF. By multiplying (50) and (51) by $e^{-j\omega_0 t}$ to eliminate the time-varying rotational component, the SS-IPT system voltage equations in the RRF can be obtained as (52) and (53). The subscript 'dq' denotes the complex form composed of the d- and q-axis components (e.g., $I^e_{tx,dq} = I^e_{tx,d} + jI^e_{tx,q}$).

$$V_e e^{j\omega_0 t} = \Bigg[R_{tx} I^e_{tx,dq} + \left(L_{tx} + \frac{1}{\omega_0^2 C_{tx}}\right)\frac{dI^e_{tx,dq}}{dt} + j\left(\omega_0 L_{tx} - \frac{1}{\omega_0 C_{tx}}\right) I^e_{tx,dq} - j\omega_0 M I^e_{rx,dq}\Bigg] e^{j\omega_0 t} \tag{50}$$

$$j\omega_0 M I^e_{tx,dq} e^{j\omega_0 t} = \Bigg[\left(L_{rx} + \frac{1}{\omega_0^2 C_{rx}}\right)\frac{dI^e_{rx,dq}}{dt} + R_{rx} I^e_{rx,dq} + j\left(\omega_0 L_{rx} - \frac{1}{\omega_0 C_{rx}}\right) I^e_{rx,dq} + R_L I^e_{rx,dq}\Bigg] e^{j\omega_0 t} \tag{51}$$

$$V_e = \Bigg[R_{tx} I^e_{tx,dq} + \left(L_{tx} + \frac{1}{\omega_0^2 C_{tx}}\right)\frac{dI^e_{tx,dq}}{dt} + j\left(\omega_0 L_{tx} - \frac{1}{\omega_0 C_{tx}}\right) I^e_{tx,dq} - j\omega_0 M I^e_{rx,dq}\Bigg] \tag{52}$$

$$j\omega_0 M I^e_{tx,dq} = \Bigg[\left(L_{rx} + \frac{1}{\omega_0^2 C_{rx}}\right)\frac{dI^e_{rx,dq}}{dt} + R_{rx} I^e_{rx,dq} + j\left(\omega_0 L_{rx} - \frac{1}{\omega_0 C_{rx}}\right) I^e_{rx,dq} + R_L I^e_{rx,dq}\Bigg] \tag{53}$$

By separating the real and imaginary parts of the voltages and currents, the differential equations for the d-axis and q-axis currents can be derived as follows.

$$\frac{dI^e_{tx,d}}{dt} = \frac{1}{L'_{tx}}\Bigg[V_e - R_{tx} I^e_{tx,d} + \left(\omega_0 L_{tx} - \frac{1}{\omega_0 C_{tx}}\right) I^e_{tx,q} - \omega_0 M I^e_{rx,q}\Bigg] \tag{54}$$

$$\frac{dI^e_{tx,q}}{dt} = \frac{1}{L'_{tx}}\Bigg[-R_{tx} I^e_{tx,q} - \left(\omega_0 L_{tx} - \frac{1}{\omega_0 C_{tx}}\right) I^e_{tx,d} + \omega_0 M I^e_{rx,d}\Bigg] \tag{55}$$

$$\frac{dI^e_{rx,d}}{dt} = \frac{1}{L'_{rx}}\Bigg[-\omega_0 M I^e_{tx,q} - (R_{rx} + R_{Leq}) I^e_{rx,d} + \left(\omega_0 L_{rx} - \frac{1}{\omega_0 C_{rx}}\right) I^e_{rx,q}\Bigg] \tag{56}$$

$$\frac{dI^e_{rx,q}}{dt} = \frac{1}{L'_{rx}}\Bigg[\omega_0 M I^e_{tx,d} - (R_{rx} + R_{Leq}) I^e_{rx,q} - \left(\omega_0 L_{rx} - \frac{1}{\omega_0 C_{rx}}\right) I^e_{rx,q}\Bigg] \tag{57}$$

where L'_{tx} and L'_{rx} represent $L_{tx} + 1/(\omega_0^2 C_{tx})$ and $L_{rx} + 1/(\omega_0^2 C_{rx})$, respectively. Assuming zero initial conditions for all states and applying the Laplace transform, Laplace-domain models for the d-axis and q-axis currents can be obtained as shown in (58)–(61).

$$I^e_{tx,d} = \frac{1}{sL'_{tx} + R_{tx}}\Bigg[V_e + \left(\omega_0 L_{tx} - \frac{1}{\omega_0 C_{tx}}\right) I^e_{tx,q} - \omega_0 M I^e_{rx,q}\Bigg] \tag{58}$$

$$I^e_{tx,q} = \frac{1}{sL'_{tx} + R_{tx}}\Bigg[-\left(\omega_0 L_{tx} - \frac{1}{\omega_0 C_{tx}}\right) I^e_{tx,d} + \omega_0 M I^e_{rx,d}\Bigg] \tag{59}$$

$$I^e_{rx,d} = \frac{1}{sL'_{rx} + R_{rx} + R_{Leq}} \left[\left(\omega_0 L_{rx} - \frac{1}{\omega_0 C_{rx}} \right) I^e_{rx,q} - \omega_0 M I^e_{tx,q} \right] \tag{60}$$

$$I^e_{rx,q} = \frac{1}{sL'_{rx} + R_{rx} + R_{Leq}} \left[- \left(\omega_0 L_{rx} - \frac{1}{\omega_0 C_{rx}} \right) I^e_{rx,q} + \omega_0 M I^e_{tx,d} \right] \tag{61}$$

In the RRF model, the tuning capacitors are transformed into equivalent inductors with inductances of $1/(\omega_0^2 C_{tx})$ and $1/(\omega_0^2 C_{rx})$ during the modeling process. Consequently, the capacitor states cannot remain as independent state variables in the RRF.

In single-phase IPT systems, the quadrature component required for dq transformation is not physically available and must therefore be synthetically generated. In practical implementations, this can be achieved using digital phase-shifting techniques applied to the sampled waveform, producing a 90° phase-shifted virtual signal. The RRF formulation assumes a known operating frequency for the synchronous transformation. When frequency control is employed, the transformation can be updated according to the instantaneous inverter operating frequency, ensuring synchronization between the rotating reference frame and the system dynamics.

The RRF formulation is derived under the FHA and assumes dominance of the fundamental component. Because the RRF model represents the system in terms of fundamental phasor quantities in a synchronous reference frame and eliminates oscillatory carrier components, its accuracy may degrade under operating conditions where higher-order harmonics become significant, such as hard-switching operation or severe waveform distortion.

It should be noted that this limitation originates from the fundamental harmonic approximation itself. Accordingly, all three modeling approaches rely on the FHA and sufficiently high-quality-factor operation to ensure dominance of the fundamental component. Their accuracy may be affected under conditions such as significant detuning from resonance, low-quality-factor behavior with increased harmonic distortion, or rapid parameter variations relative to the envelope dynamics.

III. Structural Comparison of Dynamic Models

The previous section presented the modeling procedures of the SS-IPT system based on the EDF, GSSA, and RRF approaches and derived their corresponding dynamic models. This section provides a comparative analysis of these three modeling frameworks. The structural comparisons are derived from the SS-IPT topology considered in this study. While the qualitative insights regarding modeling trade-offs may extend to other resonant compensation networks under similar fundamental harmonic assumptions, the quantitative results are specific to the SS configuration analyzed here. Although EDF, GSSA, and RRF are derived using different mathematical formulations, the comparison is conducted based on a unified SS-IPT equivalent circuit, identical system parameters, and consistent rectifier approximations to ensure a fair evaluation framework.

TABLE I
RRF Model of the Passive Components

Component	Model	d-axis	q-axis
Inductor	Voltage source	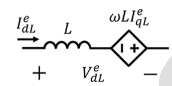	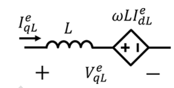
	Current source	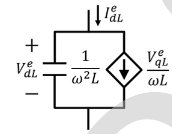	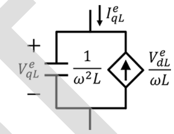
Capacitor	Voltage source	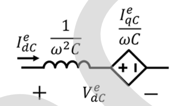	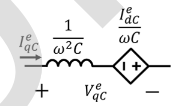
	Current source	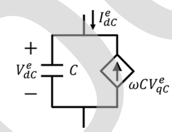	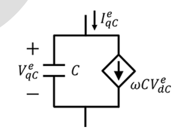
Resistor		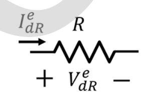	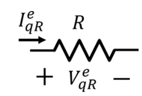

A. Generality

IPT systems incorporate a variety of compensation structures, including the series–series (SS) topology as well as series–parallel (SP), parallel–series (PS), LCCL–S, and LCL–LCL configurations. Therefore, it is important to have a modeling approach that is applicable to a wide range of resonant topologies under the fundamental harmonic assumption. Because the EDF, GSSA, and RRF models are all formulated directly from the voltage equations of the inductors and capacitors, they can be readily applied to any converter system in which the FHA is valid. In other words, these modeling approaches are applicable not only to unidirectional IPT systems but also to resonant converters and bidirectional IPT systems in which higher-order harmonics are not dominant relative to the fundamental component.

As the number of capacitors and inductors in the resonant network increases, the overall system order becomes higher, thereby increasing the mathematical complexity of the model. To simplify the modeling process, S. Lee generalized the RRF formulation by decomposing the system into passive component-level submodels as shown in Table I [51]. In this table, the voltage-source and current-source forms of the RRF models are expressed as dependent voltage and current sources, respectively. The two forms are equivalent and can be corresponding passive-component RRF models listed in Table I, the d- and q-axis RRF models of the IPT system can be converted into each other using standard source transformation. By replacing the inductors and capacitors in the circuit with the systematically constructed. This modular formulation enables straightforward extension of the RRF modeling approach to a wide range of resonant IPT topologies.

B. Block Diagram

A block-diagram representation provides an intuitive visualization of the model structure and the mutual interactions between the state variables. Fig. 4 illustrates the block diagrams of the SS-IPT system derived from the EDF, GSSA, and RRF models. In all three cases, the mutual inductance M is explicitly retained and appears as a mutual-coupled path between the transmitter and receiver resonant tanks, reflecting the underlying electromagnetic interaction.

However, in both the EDF and GSSA models, the cross-coupling terms explicitly appear as constant gains of $\pm\omega_0$. This occurs because these models remain in the SRF, where the resonant states are represented using sinusoidal basis functions. Although the transformation separates the resonant tank dynamics into orthogonal components, it does not remove the underlying carrier. Consequently, the time-derivative operators inherently generate ω_0-scaled coupling terms.

In contrast, the RRF model eliminates the explicit ω_0 coupling through a synchronous transformation into the rotating dq-frame. As a result, the sinusoidal carrier is completely removed, and the stored energy transfer between the d- and q-axes is governed not by basis-function derivatives but by the net reactive impedance imbalance of the resonant tanks. When the system is perfectly tuned for both the transmitter and receiver (i.e., $\omega_0 L_{tx} = 1/(\omega_0 C_{tx})$ and $\omega_0 L_{rx} = 1/(\omega_0 C_{rx})$), the d- and q-axes become fully decoupled. Under this condition, the RRF model clearly reveals that the dominant power transfer occurs through the d-axis transmitter to q-axis receiver.

C. Control-Oriented Interpretation

From a control-design standpoint, the block diagrams of all three models clearly highlight the feedback and feedforward pathways, making them applicable for controller development. The EDF model, however, represents the full system dynamics directly in the time domain and therefore exhibits the highest structural complexity. This makes EDF particularly suitable for detailed time-domain simulation rather than analytical controller synthesis.

The GSSA model reduces the complexity through an averaging process, yet its block diagram still preserves the separated capacitor and inductor dynamics within the SRF. Consequently, the plant remains cross-coupled, and its control-design complexity is still relatively high.

In contrast, the RRF model leverages the RRF transformation, in which the capacitive dynamics are not removed but are absorbed into the modified inductive terms of the plant and into the net reactive impedance that governs cross-axis coupling. As a result, this model yields the simplest block-diagram representation among the three approaches, where the plant effectively behaves as a series LR circuit in steady-state operation. Therefore, from a structural and representation standpoint, the RRF model offers advantages for controller-oriented analysis by eliminating oscillatory carrier dynamics and reducing the system to a lower-order real-axis plant. However, the present study does not include explicit controller implementation or robustness analysis, and the suitability assessment is based on structural characteristics rather than closed-loop performance validation.

It should be noted that the apparent reduction in model order observed in the RRF formulation results from the absorption of capacitor dynamics into modified inductive terms through the synchronous reference-frame transformation. In contrast, EDF and GSSA retain explicit capacitor state variables in the stationary reference frame. Therefore, the relative simplicity of the RRF model from a control-design perspective does not arise from the removal of physical dynamics, but rather from differences in state representation. In other words, the control-oriented structural simplicity stems from the level of modeling abstraction rather than a reduction in underlying system dynamics.

Under detuned operation, the predictive fidelity of all three models may be affected as the dominance of the fundamental component weakens and higher-order harmonic effects become more pronounced. In the EDF and GSSA formulations, this may manifest as increased envelope deviation due to reduced validity of the fundamental harmonic approximation. In the RRF formulation, detuning additionally increases the reactive imbalance term, leading to stronger cross-axis coupling and reduced structural decoupling. Thus, while all models remain structurally valid, both their transient envelope accuracy and control-oriented simplicity may diminish as the system deviates from resonance.

TABLE II
CIRCUIT PARAMETERS OF THE SS-IPT SYSTEM

Parameter	Value	Parameter	Value
Operating frequency	85 kHz	L_{rx}	45 μH
V_{DC}	210 V	C_{rx}	90 nF
L_{tx}	34 μH	R_{rx}	64 mΩ
C_{tx}	126 nF	C_f	50 μF
R_{tx}	66 mΩ	R_f	1 mΩ
k	0.2	R_L (R_{Leq})	4 Ω (3.24 Ω)

IV. SIMULATION-BASED PERFORMANCE EVALUATION

In this section, the performance of the EDF, GSSA, and RRF models is compared using PLECS simulations. The circuit parameters of the SS-IPT system used in the simulations are listed in Table II. To ensure a fair baseline for comparing the numerical fidelity of the EDF, GSSA, and RRF methodologies, the system parameters are selected to represent typical high-efficiency operating conditions. The circuit design criteria focus on high-quality-factor resonant tanks operating under near-zero-voltage-switching conditions with a slight detuning margin. A simulation model was constructed based on the equations of the three models presented in Section II and the block diagrams shown in Fig. 5.

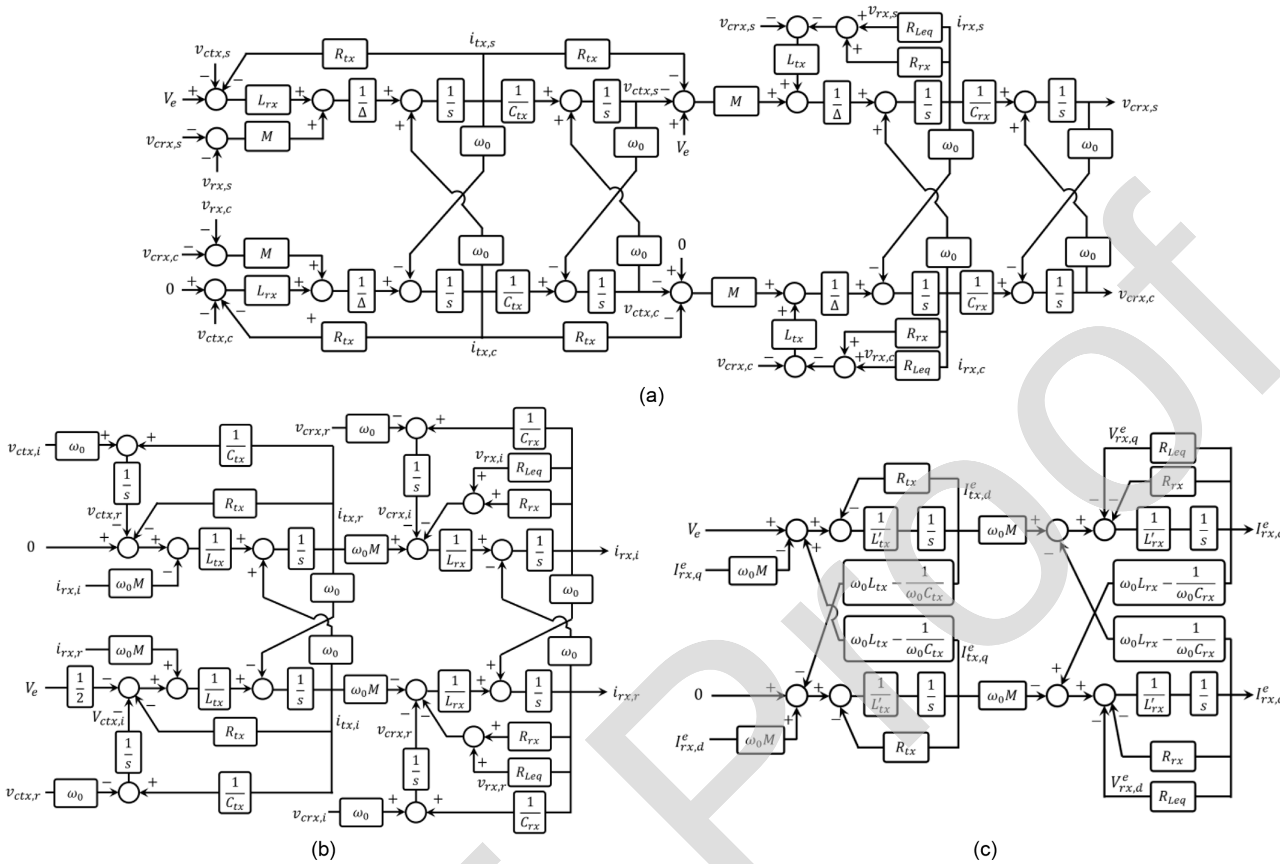

Fig. 5. Block diagrams of the SS-IPT system: (a) EDF, (b) GSSA, and (c) RRF models.

D. Full-Wave Rectifier Resistive Approximation

When the rectifier is approximated as a purely resistive load, the dynamic behavior of the DC-link cannot be accurately represented. Such a resistive approximation neglects the nonlinear switching behavior of the rectifier, the conduction interval of the diodes, and the charging and discharging overshoot, and the variation of the rectifier input impedance under load and coupling changes—are not captured. To address these modeling needs, a two-step analysis is employed. First, the EDF model is validated against switching simulations to capture high-fidelity rectifier dynamics. Second, a full-wave resistive rectifier approximation is adopted as a common baseline to ensure a consistent comparison of the EDF, GSSA, and RRF models, focusing strictly on their dynamic tracking capabilities.

Regarding the second step, using the FHA for the rectifier input while explicitly modeling the rectifier capacitor C_f and its ESR R_f in Fig. 1 provides a more balanced representation. Although the square-wave nature of the rectifier input voltage is simplified to a sinusoid through the FHA, the inclusion of C_f and R_f preserves the essential energy-storage and damping dynamics of the DC-link. This approach significantly improves transient fidelity while maintaining a tractable model structure, making it highly suitable for dynamic performance prediction. Fig. 6 shows the full receiver-current dynamics of the SS-IPT system along with the envelope predicted by the EDF model when the load resistance R_L is changed from 12 Ω to 4 Ω. The EDF model is constructed using (9)–(18), where the rectifier capacitor C_f is incorporated. It should be noted that the EDF model incorporating the rectifier-capacitor dynamics closely tracks the nonlinear envelope response of the SS-IPT system, indicating that the dominant nonlinear effects introduced by the rectifier are well approximated.

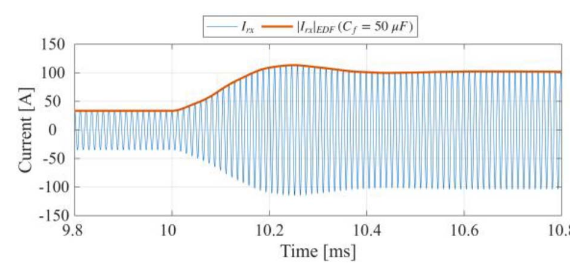

Fig. 6. Dynamic responses of the receiver current and the EDF model envelope under a load change from 12 Ω to 4 Ω.

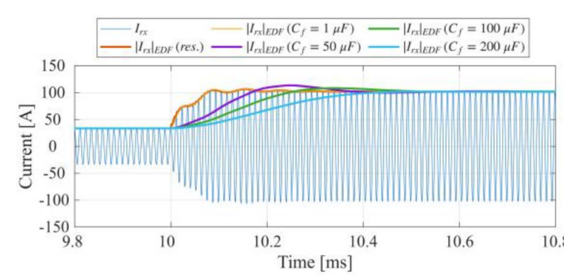

Fig. 7. Comparison of EDF-model envelopes obtained with rectifier-capacitor modeling and with a resistive rectifier approximation.

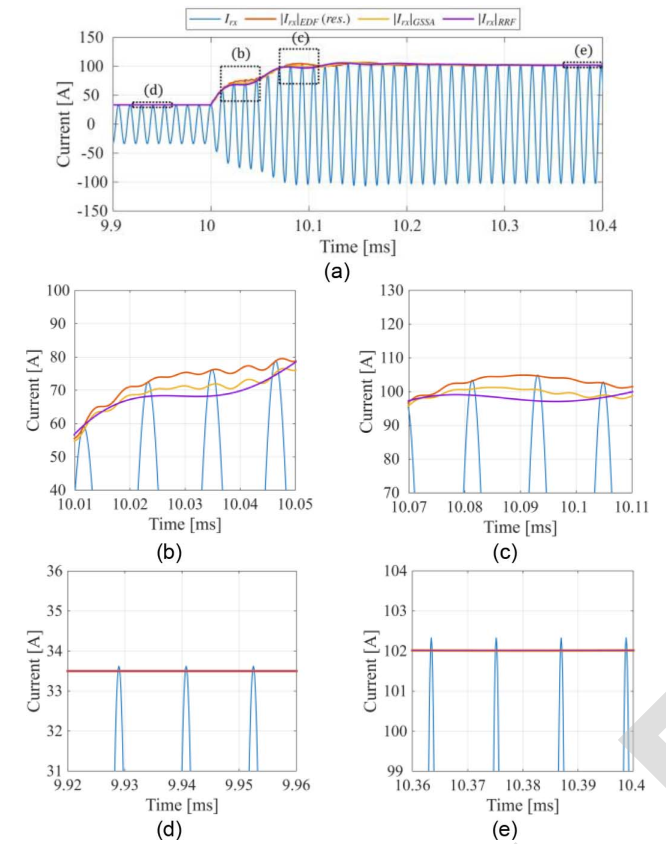

Fig. 8. Transient response of the receiver current envelopes of the EDF, GSSA, and RRF models under a step change in R_{Leq} from 9.72 Ω to 3.24 Ω: (a) Full dynamics; (b), (c) zoomed-in transient response; (d) pre-transition steady state; (e) post-transition steady state.

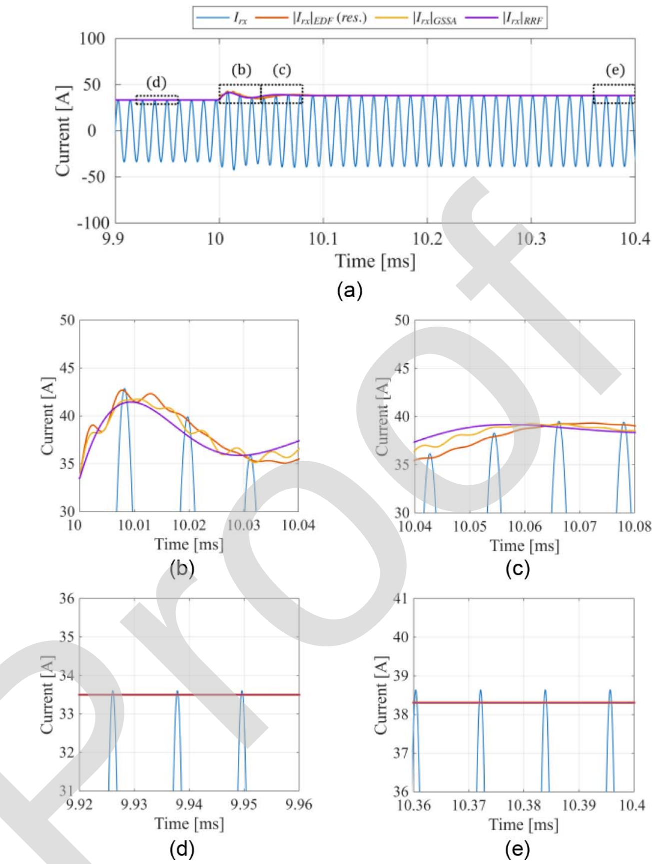

Fig. 9. Transient response of the receiver current envelopes of the EDF, GSSA, and RRF models under a step change in k from 0.2 to 0.3: (a) Full dynamics; (b), (c) zoomed-in transient response; (d) pre-transition steady state; (e) post-transition steady state.

Fig. 7 compares the receiver-current envelope predicted by the EDF model when the rectifier is approximated as an equivalent resistance with the envelopes obtained when the rectifier capacitor C_f is explicitly included. The equivalent load resistance R_{Leq} is changed from 9.72 Ω to 3.24 Ω, corresponding to a load change from 12 Ω to 4 Ω according to (21). The blue line represents the receiver current of the SS-IPT system, while the orange line shows the EDF envelope under the resistive rectifier approximation. The yellow, purple, green, and cyan lines correspond to the EDF envelopes obtained with $C_f = 1$ μF, 50 μF, 100 μF, and 200 μF, respectively.

It can be observed that the steady-state envelope values remain identical regardless of whether the rectifier capacitor is included. However, as C_f increases, the transient response becomes slower, leading to increased settling-time deviation between the actual rectifier-capacitor system and the resistive approximation. This result highlights the influence of the rectifier-capacitor dynamics on transient behavior and clarifies the limitations of the equivalent resistive approximation.

Having established in Fig. 6 that the EDF formulation accurately captures the nonlinear envelope behavior when the rectifier capacitor is included, Fig. 7 further examines the effect of simplifying the rectifier to an equivalent resistance. This intermediate analysis provides a basis for the subsequent cross-model comparison, which is conducted under the resistive rectifier approximation to ensure a consistent evaluation framework.

This analysis highlights the influence of rectifier representation on transient response. To ensure consistency in cross-model comparison, the equivalent resistive approximation is uniformly applied across all three modeling approaches. The inclusion of rectifier-capacitor dynamics in the EDF formulation is therefore presented as a complementary analysis to demonstrate its extended modeling capability rather than to bias the comparative evaluation.

E. Transient Response

The transient performance of the three models was evaluated for the following two cases: when R_{Leq} stepped from 9.72 Ω to 3.24 Ω, and when k stepped from 0.2 to 0.3. The inverter duty cycle was fixed at 0.5. Fig. 8(a) shows the full transient dynamics of the receiver current envelope for the three models under the load-change condition, and Fig. 8(b) and Fig. 8(c) present the corresponding zoomed-in view. The blue line shows the receiver current, while the orange, yellow, and purple lines represent the corresponding current envelopes predicted by the EDF, GSSA, and RRF models, respectively.

Although all three models are derived under the same FHA assumptions, a small $2\omega_0$ ripple is observed in the EDF and GSSA models, whereas it is not observed in the RRF model. This difference arises from the way each model represents the

TABLE III
COMPARISON OF DYNAMIC MODEL CHARACTERISTICS

Attribute	EDF	GSSA	RRF
Model type	Full dynamic model	Averaged dynamic model	Phasor-based dynamic model
Harmonic representation	Fundamental only	Fundamental only	Fundamental only
Transient accuracy	High	Medium	Low
Steady-state accuracy	High	High	High
Dynamic mutual coupling	Fully preserved	Partially smoothed	Replaced by steady-state coupling
$2\omega_0$ ripple in envelope	Present	Present	Removed
Computational burden	High	Medium	Low
Control-oriented suitability	Medium	High	Very high
Intended use	High-fidelity analysis	Control-oriented dynamic analysis	Control design and real-time implementation

fundamental waveform. In the EDF and GSSA models, the system is formulated in the SRF, where the sinusoidal current is expressed using two orthogonal time-domain components (e.g., sine–cosine or cosine–sine pairs). When a sinusoidal waveform is represented using orthogonal time-domain components, the representation inherently preserves the positive- and negative-frequency spectral components that any real time-domain signal contains. Consequently, these paired components emerge in the orthogonal state variables as a DC-like term and a small $2\omega_0$ oscillation, although the physical current contains only the fundamental component. In contrast, the RRF model employs a phasor-based representation of the fundamental component, in which only the positive-frequency term of the sinusoidal waveform is retained. The corresponding negative-frequency component— responsible for producing the $2\omega_0$ term in stationary-frame representations—is removed during the modeling process. As a result, the RRF state variables evolve smoothly without the $2\omega_0$ ripple observed in the EDF and GSSA models. The maximum envelope error rates of the EDF, GSSA, and RRF models during the transient were 0.24%, 4.12%, and 7.31%, respectively.

Fig. 9(a) shows the full transient dynamics of the receiver current under a step change in k from 0.2 to 0.3, while Fig. 9(b) and Fig. 9(c) provide zoomed-in views. The transient behavior is similar to that observed in the load-step case. The EDF and GSSA models exhibit a small $2\omega_0$ ripple, whereas the RRF model remains ripple-free. The maximum envelope error rates of the EDF, GSSA, and RRF models during the transient are 1.24%, 2.19%, and 4.82%, respectively.

Therefore, EDF provides the highest transient envelope accuracy under the examined load-step conditions because it preserves the full fundamental-frequency envelope dynamics of the coupled system. As a result, EDF more accurately captures the transient envelope behavior associated with rapid variations in coil currents, while steady-state predictions remain comparable across the three models. GSSA maintains the same structural form as EDF but applies a periodic averaging operation that partially smooths the system dynamics. Although the overall coupling behavior is preserved, the averaging process attenuates certain fast transient components, leading to moderately lower accuracy compared to EDF. In contrast, the RRF model relies on a phasor-based approximation that represents the system in terms of slowly varying fundamental components. This phasor formulation removes the dynamic cross-coupling introduced by the mutual inductance. Consequently, the RRF model offers the least accurate transient prediction among the three, especially when the transient interaction between the coils changes rapidly.

F. Steady-State Response

Fig. 8(d) and 8(e) illustrate the steady-state responses before and after the load transition, respectively. In both operating conditions, the EDF, GSSA, and RRF models converge to the same steady-state value, yielding deviations of 0.36% and 0.31% from the actual receiver current amplitude. These discrepancies primarily arise from the modeling of the inverter output voltage. In the actual system, the transmitter coil is driven by a square-wave voltage containing non-negligible harmonic components, whereas all analytical models employ the FHA, representing the inverter output solely by its fundamental component. Consequently, the deviation between the analytical predictions and the actual system depends on the harmonic content of the inverter output voltage and varies according to its spectral composition. Furthermore, when a rectifier is included in the system, additional harmonic components are introduced, which can further influence the steady-state deviation depending on the rectifier topology and operating conditions.

Fig. 9(d) and (e) illustrate the steady-state responses before and after the k transition, respectively. The steady-state behavior is similar to that observed in the load-variation case. In both operating conditions, the EDF, GSSA, and RRF models converge to the same steady-state value, yielding deviations of 0.36% and 0.86% from the actual receiver current amplitude.

G. Comparative Summary of Model Performance

Table III summarizes the principal characteristics and performance of the EDF, GSSA, and RRF models. The EDF model represents the full time-domain dynamics of the system, preserving complete mutual-inductance coupling and providing the highest transient accuracy. However, this fidelity limits its suitability for control-oriented implementation.

The GSSA model uses an averaged dynamic formulation that reduces high-frequency artifacts while preserving the dominant fundamental dynamics. Consequently, it offers moderate transient accuracy with substantially lower mathematical complexity. The GSSA model also maintains high steady-state accuracy, making it well suited for control-oriented dynamic analysis that requires a balance between fidelity and efficiency.

The RRF model adopts a phasor-based dynamic representation that describes the system through slowly varying fundamental components. This formulation provides the highest suitability for control design and real-time implementation. However, the simplified treatment of dynamic mutual coupling reduces its transient accuracy, even though its steady-state accuracy remains high.

From a computational standpoint, structural differences among the models influence numerical efficiency. The EDF formulation retains coupled envelope states and nonlinear interactions, which may increase solver effort and reduce Jacobian sparsity during transient simulation. The GSSA model benefits from averaging, mitigating high-frequency effects and improving numerical conditioning. In contrast, the RRF model eliminates explicit oscillatory carrier components, typically resulting in a lower apparent model order and faster simulation. These aspects may be relevant when computational constraints are considered.

V. Conclusion

This review examined three representative dynamic modeling approaches for series–series compensated IPT systems: the EDF, GSSA, and RRF models. All three models were formulated on a common FHA-based equivalent circuit, providing a consistent basis for analyzing their dynamic characteristics and the modeling assumptions embedded in each approach.

Based on this formulation, a comparative evaluation was performed to assess their ability to represent the transient and steady-state behaviors of the IPT system. The EDF model, which retains the full time-domain dynamics, demonstrated the highest transient envelope fidelity under the examined operating conditions. The GSSA model preserved the dominant fundamental behavior through its averaged formulation and yielded moderately accurate transient responses. The RRF model, formulated in the synchronous reference frame, may facilitate control-oriented analysis from a structural standpoint, although it exhibits reduced transient envelope accuracy due to its phasor-based simplification. Simulation results under load-transition conditions confirmed these distinctions and showed that the small steady-state deviations observed across all three models originate from the FHA representation of the inverter output and the omission of rectifier-induced harmonics rather than from limitations of the modeling frameworks themselves.

Overall, the analysis presented in this paper clarifies the essential trade-offs among the EDF, GSSA, and RRF dynamic models and offers practical guidance for selecting an appropriate modeling approach according to the required level of dynamic fidelity and control-design objectives.

References

[1] W. Liu, J. Lu, C. C. Mi, and K. T. Chau, "Integrated sensorless wireless charging using symmetric high-order network for multistorey car packs," *IEEE Trans. Power Electron.*, vol. 39, no. 8, pp. 10568–10581, Aug. 2024.

[2] C. Wang et al., "A misalignment-adaptive wireless charging system for inspection robots," *IEEE Trans. Transport. Electrific.*, vol. 11, no. 6, pp. 13490–13499, Dec. 2025.

[3] N. Mirković, A. Delgado, P. Alou, and M. Vasić, "24 kW single-stage three-phase inductive power transfer charger for EV applications based on matrix converter and DD^{2}Q coil topology," *IEEE Trans. Power Electron.*, vol. 41, no. 2, pp. 2991–3010, Feb. 2026.

[4] C. C. Chen and Y. K. Chu, "Hall sensor-based remote control in twin square compensation magnetic module design for dynamic misalignment in underwater wireless power transfer for AUVs," *IEEE Sensors J.*, vol. 25, no. 17, pp. 33810–33821, Sep. 2025.

[5] C. Ma, X. Qu, Z. Guo, and L. Tan, "Four-switch buck-boost integrated bridge for bidirectional inductive power transfer with hybrid energy storage system," *IEEE Trans. Ind. Electron.*, vol. 72, no. 9, pp. 9028–9038, Sep. 2025.

[6] K. Chen et al., "A high-interoperability optimal frequency control method for the AGV dynamic wireless charging systems without communication," *IEEE Trans. Power Electron.*, vol. 39, no. 3, pp. 3797–3808, Mar. 2024.

[7] A. Aktas et al., "Medium-duty delivery truck integrated bidirectional wireless power transfer system with grid and stationary energy storage system connectivity," *IEEE Trans. Emerg. Sel. Topics Power Electron.*, vol. 12, no. 5, pp. 5364–5382, Oct. 2024.

[8] J. Kim et al., "Development of 1-MW inductive power transfer system for a high-speed train," *IEEE Trans. Ind. Electron.*, vol. 62, no. 10, pp. 6242–6250, Oct. 2015.

[9] G. Lee et al., "Electromagnetic field tests of a 1-MW wireless power transfer system for light rail transit," *Energies*, vol. 14, no. 4, pp. 1–15, Feb. 2021.

[10] E. Asa et al., "Overview of high-power wireless charging systems and analysis of polyphase wireless charging system phase winding and resonant tuning network connection configurations," *IEEE Trans. Transport. Electrific.*, vol. 11, no. 2, pp. 6700–6718, Apr. 2025.

[11] E. Choi, S. Lee, and S. H. Lee, "Optimal tuning of series-series tuned inductive power transfer system," *J. Electr. Eng. Technol.*, vol. 20, pp. 4315–4327, Jun. 2025.

[12] F. Wang et al., "Enhancing misalignment tolerance in hybrid wireless power transfer system with integrated coupler via frequency tuning," *IEEE Trans. Power Electron.*, vol. 39, no. 9, pp. 11885–11899, Sep. 2024.

[13] R. Xie et al., "A series of dual-frequency hybrid topologies with vertical and horizontal misalignment tolerance performance in inductive power transfer systems," *IEEE Trans. Transport. Electrific.*, vol. 11, no. 4, pp. 10203–10211, Aug. 2025.

[14] Z. Sun et al., "Analysis and design of a 6.78 M wireless power transfer system with strong misalignment tolerance based on simplified impedance trajectory tracing," *IEEE Trans. Ind. Electron.*, vol. 71, no. 10, pp. 13470–13475, Oct. 2024.

[15] W. Zhang, S.-C. Wong, C. K. Tse, and Q. Chen, "Analysis and comparison of secondary series- and parallel-compensated inductive power transfer systems operating for optimal efficiency and load-independent voltage-transfer ratio," *IEEE Trans. Power Electron.*, vol. 29, no. 6, pp. 2979–2990, Jun. 2014.

[16] Y. H. Sohn et al., "General unified analyses of two-capacitor inductive power transfer systems: Equivalence of current-source SS and SP compensations," *IEEE Trans. Power Electron.*, vol. 30, no. 11, pp. 6030–6045, Nov. 2015.

[17] X. Qu, Y. Jing, H. Han, S.-C. Wong, and C. K. Tse, "Higher order compensation for inductive-power-transfer converters with constant-voltage or constant-current output combating transformer parameter constraints," *IEEE Trans. Power Electron.*, vol. 32, no. 1, pp. 394–405, Jan. 2017.

[18] G. A. Covic and J. T. Boys, "Inductive power transfer," *Proc. IEEE*, vol. 101, no. 6, pp. 1276–1289, Jun. 2013.

[19] A. K. Swain, M. J. Neath, U. K. Madawala, and D. J. Thrimawithana, "A dynamic multivariable state-space model for bidirectional inductive power transfer systems," *IEEE Trans. Power Electron.*, vol. 27, no. 11, pp. 4772–4780, Nov. 2012.

[20] A. Safaee and K. Woronowicz, "Time-domain analysis of voltage-driven series–series compensated inductive power transfer topology," *IEEE Trans. Power Electron.*, vol. 32, no. 7, pp. 4981–5003, Jul. 2017.

[21] S. Lee, B. Choi, and C. T. Rim, "Dynamics characterization of the inductive power transfer system for online electric vehicles by Laplace phasor transform," *IEEE Trans. Power Electron.*, vol. 28, no. 12, pp. 5902–5909, Dec. 2013.

[22] Z. U. Zahid et al., "Modeling and control of series–series compensated inductive power transfer system," *IEEE Trans. Emerg. Sel. Topics Power Electron.*, vol. 3, no. 1, pp. 111–123, Mar. 2015.

[23] S. Das and A. K. Yadav, "Small signal modeling of LCC-S compensated multiphase inductive power transfer system using extended

describing function method," *IEEE Trans. Ind. Appl.*, vol. 61, no. 5, pp. 7431–7442, Sept./Oct. 2025.

[24] T. Ma et al., "Modeling and analysis of periodic energy control for series–series wireless power transfer system," *IEEE Trans. Power Electron.*, vol. 39, no. 4, pp. 4837–4849, Apr. 2024.

[25] C. Buccella et al., "Observer-based control of LLC DC/DC resonant converter using extended describing functions," *IEEE Trans. Power Electron.*, vol. 30, no. 10, pp. 5881–5891, Oct. 2015.

[26] D. Wu and K. Chen, "Frequency-domain analysis of nonlinear active disturbance rejection control via the describing function method," *IEEE Trans. Ind. Electron.*, vol. 60, no. 9, pp. 3906–3914, Sep. 2013.

[27] D. Zhang, H. Li, and J. Chen, "A unified dual active bridge model based on improved extended describing function with dead time compensation for electric vehicles," *IEEE Access*, vol. 12, pp. 81374–81387, 2024.

[28] H. Hao, G. A. Covic, and J. T. Boys, "An approximate dynamic model of LCL-T-based inductive power transfer power supplies," *IEEE Trans. Power Electron.*, vol. 29, no. 10, pp. 5554–5567, Oct. 2014.

[29] C. Xia et al., "Robust control for inductively coupled power transfer systems with coil misalignment," *IEEE Trans. Power Electron.*, vol. 33, no. 9, pp. 8110–8122, Sep. 2018.

[30] H. Li et al., "Duty cycle control strategy for dual-side LCC resonant converter in wireless power transfer systems," *IEEE Trans. Transport. Electrific.*, vol. 8, no. 2, pp. 1944–1955, Jun. 2022.

[31] A. Emadi, "Modeling and analysis of multiconverter DC power electronic systems using the generalized state-space averaging method," *IEEE Trans. Ind. Electron.*, vol. 51, no. 3, pp. 661–668, Jun 2004.

[32] S. R. Sanders, J. M. Noworolski, X. Z. Liu, and G. C. Verghese, "Generalized averaging method for power conversion circuits," *IEEE Trans. Power Electron.*, vol. 6, no. 2, pp. 251–259, Apr. 1991.

[33] X. Li et al., "Multifrequency model of dual active bridge resonant converters with phase-shift control," *IEEE Trans. Power Electron.*, vol. 40, no. 9, pp. 13007–13022, Sep. 2025.

[34] T. Yao et al., "A family of high step-up DC–DC converters based on enhanced boost cells with coupled inductor," *IEEE Trans. Power Electron.*, vol. 38, no. 10, pp. 12932–12945, Oct. 2023.

[35] S. Lee and S. H. Lee, "*dq* synchronous reference frame model of a series–series tuned inductive power transfer system," *IEEE Trans. Ind. Electron.*, vol. 67, no. 12, pp. 10325–10334, Dec. 2020.

[36] K. Chen and Z. Zhang, "Rotating-coordinate-based mutual inductance estimation for drone in-flight wireless charging systems," *IEEE Trans. Power Electron.*, vol. 38, no. 9, pp. 11685–11693, Sep. 2023.

[37] S. Lee and S. H. Lee, "Observer-based online parameter identification of series-series tuned inductive power transfer system," *IEEE Trans. Ind. Electron.*, vol. 72, no. 3, pp. 2927–2937, Mar. 2025.

[38] W. Hong, S. Lee, and S. H. Lee, "Sensorless control of series–series tuned inductive power transfer system," *IEEE Trans. Ind. Electron.*, vol. 70, no. 10, pp. 10578–10587, Oct. 2023.

[39] W. Hong, S. Lee, E. Choi, and S. H. Lee, "Observer-based maximum efficiency point tracking controller for a series–series tuned, 60 kHz inductive power transfer system," *IEEE Trans. Transport. Electrific.*, vol. 10, no. 3, pp. 5334–5343, Sep. 2024.

[40] S. Lee et al., "Load voltage and current observers for series–series wireless power transfer system," *IEEE Trans. Ind. Electron.*, vol. 69, no. 6, pp. 5615–5624, Jun. 2022.

[41] A. R. Fuentes, M. J. Carrizosa, and R. Ramos, "Neural network-based design of wireless power transfer systems for implantable medical devices," *IEEE Trans. Power Electron.*, vol. 41, no. 2, pp. 3011–3024, Feb. 2026.

[42] F. Amadei, M. Quercio, and F. R. Fulginei, "Recent results on the use of artificial intelligence techniques applied to wireless power transfer systems," *IEEE Access*, vol. 13, pp. 58443–58464, 2025.

[43] F. Xu et al., "Data-driven output prediction and efficiency optimization control for wireless power transfer systems," *IEEE Trans. Power Electron.*, vol. 40, no. 10, pp. 14196–14209, Oct. 2025.

[44] F. Chen et al., "Data-driven modeling of wireless power transfer systems with multiple transmitters," *IEEE Trans. Power Electron.*, vol. 35, no. 11, pp. 11363–11379, Nov. 2020.

[45] V. Ramakrishnan et al., "A comprehensive review on efficiency enhancement of wireless charging system for the electric vehicles applications," *IEEE Access*, vol. 12, pp. 46967–46994, 2024.

[46] M. Rehman et al., "A review of inductive power transfer: emphasis on performance parameters, compensation topologies and coil design aspects," *IEEE Access*, vol. 11, pp. 144978–145010, 2023.

[47] W. Zhang and C. C. Mi, "Compensation topologies of high-power wireless power transfer systems," *IEEE Trans. Veh. Technol.*, vol. 65, no. 6, pp. 4768–4778, Jun. 2016.

[48] S. Jayalath and A. Khan, "Design, challenges, and trends of inductive power transfer couplers for electric vehicles: A review," *IEEE Trans. Emerg. Sel. Topics Power Electron.*, vol. 9, no. 5, pp. 6196–6218, Oct. 2021.

[49] M. A. Ngini, C. T. Truong, and S. J. Choi, "Parameter identification for primary-side control of inductive wireless power transfer systems: A review," *IEEE Access*, vol. 13, pp. 15885–15904, 2025.

[50] R. W. Erickson and D. Maksimović, *Fundamentals of Power Electronics*, 2nd ed., New York, NY, USA: Springer-Verlag, 2001.

[51] S. Lee, "Modeling, estimation, and control of inductive power transfer systems in synchronous reference frame," Ph.D. dissertation, Dept. Electr. Comput. Eng., Univ. Seoul, Seoul, South Korea, 2025.

Sangmin Lee (Member, IEEE) received the B.S. degree in business administration and electrical and computer engineering and the Ph.D. degree in electrical and computer engineering from the University of Seoul, Korea, in 2018 and 2025, respectively. He is currently a Postdoctoral Research Fellow with San Diego State University. His research interests include wireless power transfers, high-power-density converters, and electric vehicle charging systems.

Lars Bjorndal (Student Member, IEEE) received the B.S. degree in electrical engineering from the University of Florida, in 2021. He is currently working toward the Ph.D. degree in electrical and computer engineering with San Diego State University and the University of California, San Diego. His research interests include modeling and cybersecurity for power-electronics-based power systems, with emphasis on attack and anomaly detection using data-driven and model-based methods.

Naser Vosoughi Kurdkandi (Member, IEEE) received the Ph.D. degree in electrical engineering and power electronics from the University of Tabriz, Tabriz, Iran, in 2019. From 2019 to 2020, he was a Postdoctoral Researcher with the University of Tabriz. In 2020, he joined as a Postdoctoral Researcher with Tallinn University of Technology, Tallinn, Estonia. Since 2022, he has been a Postdoctoral Research Fellow with San Diego State University, San Diego, CA, USA. His research interests include multilevel inverters, grid-connected photovoltaic inverters, DC–DC switched-capacitors and switched-inductor converters, fast charging stations for electric vehicles, battery-based energy storage systems, solid-state transformers, and induction motor drives. He has been recognized as one of the world's top 2% most-cited scientists since 2021, according to a global-citation-based ranking by Stanford University, Stanford, CA.

Ching-Ming Lai (Senior Member, IEEE) received the Ph.D. degree in electrical engineering from the National Tsing Hua University in 2010. He is the Founder of UPE-Power Technology, specializing in ODM/OEM/EMS services for power supplies and electronics circuits. He is currently a Professor with the National Chung Hsing University, he oversees the Intelligent Electric Vehicle and Green Energy Center. In 2021, he was the Director with the Intelligent Transportation Development Center. His research interests include electric vehicles, power electronics, green energy technologies, and intelligent transportations. He is recognized as a fellow of the Institution of Engineering and Technology (U.K.) and the Australian Institute of Energy. He founded and served as the Secretary General of the Taiwan EV and Green Energy Association. His achievements include numerous paper awards, acknowledgment as a top 2% scientist in Energy, and various distinguished researcher and engineer accolades. He has actively contributed to IEEE conferences, serving as an Editor for IEEE TRANSACTIONS ON VEHICULAR TECHNOLOGY and an Associate Editor for IEEE ACCESS.

Chunting Chris Mi (Fellow, IEEE) received the B.S.E.E. and M.S.E.E. degrees from the Northwestern Polytechnical University, Xi'an, China, and the Ph.D. degree from the University of Toronto, Toronto, ON, Canada, in 1985, 1988, and 2001, respectively, all in electrical engineering. He is a Distinguished Professor with the Department of Electrical and Computer Engineering and the Director of Caili and Daniel Chang Center of Electrical Drive Transportation, San Diego State University (SDSU), San Diego, USA. From 2001 to 2015, he was with the University of Michigan, Dearborn. His research interests include electric drives, power electronics, electric machines, electrical and hybrid vehicles, wireless power transfers, and power electronics. In 2019, he received the Inaugural IEEE Power Electronics Emerging Technology Award. In 2022, he received the Albert W. Johnson Research Lectureship and was named the Distinguished Professor, the highest honor given to an SDSU Faculty Member, and only one award is given each year. In 2023, he received the IEEE PELS Vehicle and Transportation Systems Achievement Award, the IEEE Transactions on Industry Applications Best Paper Award, and the SDSU Innovator of the Year Award. In 2024, he received the prestigious Alumni Distinguished Faculty Award from SDSU. Most recently, he received the Wang Family Excellence Award from the California State University System.